



Meandering due to large eddies and the statistically self-similar dynamics of quasi-two-dimensional jets

Julien R Landel, C. Caulfield, Andrew Woods

► To cite this version:

Julien R Landel, C. Caulfield, Andrew Woods. Meandering due to large eddies and the statistically self-similar dynamics of quasi-two-dimensional jets. *Journal of Fluid Mechanics*, 2012, 692, pp.347-368. <10.1017/jfm.2011.518>. <hal-04651349>

HAL Id: hal-04651349

<https://hal.science/hal-04651349v1>

Submitted on 17 Jul 2024

HAL is a multi-disciplinary open access archive for the deposit and dissemination of scientific research documents, whether they are published or not. The documents may come from teaching and research institutions in France or abroad, or from public or private research centers.

L'archive ouverte pluridisciplinaire **HAL**, est destinée au dépôt et à la diffusion de documents scientifiques de niveau recherche, publiés ou non, émanant des établissements d'enseignement et de recherche français ou étrangers, des laboratoires publics ou privés.



HAL Authorization

Meandering due to large eddies and the statistically self-similar dynamics of quasi-two-dimensional jets

JULIEN R. LANDEL^{1,2}, C. P. CAULFIELD^{1,2} and A. W. WOODS¹

¹BP Institute, University of Cambridge, Madingley Road, Cambridge, CB3 0EZ, UK

²Department of Applied Mathematics and Theoretical Physics, University of Cambridge, Centre for Mathematical Sciences, Wilberforce Road, Cambridge, CB3 0WA, UK

Author accepted version, 18 November 2011

Abstract

We investigate experimentally the structure of quasi-two-dimensional plane turbulent jets discharged vertically from a slot of width d into a fluid confined between two relatively close rigid boundaries with gap $W \sim O(d)$. At large vertical distances $z \gg W$ the jet structure consists of a meandering core with large counter-rotating eddies which develop on alternate sides of the core. Using particle image velocimetry, we observe an inverse cascade typical of quasi-two-dimensional turbulence where both the core and the eddies grow linearly with z and travel at an average speed proportional to $z^{-1/2}$. However, although the present study concerns quasi-two-dimensional confined jets, the jets are self-similar and the mean properties are consistent with both experimental results and theoretical models of the time-averaged properties of fully unconfined planar two-dimensional jets. We believe that the dynamics of the interacting core and large eddies accounts for the Gaussian profile of the mean vertical velocity as shown by the spatial statistical distribution of the core and eddy structure. The lateral excursions (caused by the propagating eddies) of this high-speed central core produces a Gaussian distribution for the time-averaged vertical velocity. In addition, we find that approximately 75% of the total momentum flux of the jet is contained within the core. The eddies travel substantially slower (at approximately 25% of the maximum speed of the core) at each height and their growth is primarily attributed to entrainment of ambient fluid. The frequency of occurrence of the eddies decreases in a step-wise manner due to merging, with a well-defined minimum value of the corresponding Strouhal number $St \geq 0.07$.

1 Introduction

The study of turbulent plane jets is relevant to a wide variety of problems where both a qualitative and quantitative knowledge of the concentration in time and space of tracers transported by the jet is needed (Kotsovinos, 1975). In many industrial applications, effluents, waste or even pollutants are released into large basins such as lakes, or oceans. The source of the discharge can be rivers (see for example Rowland, Stacey & Dietrich, 2009, and references) or multiport diffusers (see Jirka, 2006, for an extensive study). In both situations, characteristic horizontal dimensions are much larger than the fluid-layer thickness and the flow develops in a confined environment. Early experimental studies of bounded plane jets by Foss & Jones (1968) and Holdeman & Foss (1975) showed the influence of secondary flows on the mean flow. However, as Giger, Dracos & Jirka (1991) and Dracos, Giger & Jirka (1992) pointed out, these secondary flows disappear beyond a distance of ten flow thicknesses. The present work focuses on this far field region ($z/W \geq 10$, where z is in the flow direction and W is the fluid-layer thickness) where the jet has

been observed to meander due to the development of large eddies which grow on its sides. In this far field region, the initially planar two-dimensional jet is referred to as a quasi-two-dimensional jet because of the influence of the spanwise restriction on the flow. The key characteristic of quasi-two-dimensional jets is the development of an instability (see Chen & Jirka, 1998, for a linear stability analysis of shallow water jets) featuring large planar counter-rotating eddies. Dracos *et al.* (1992) noted that the spanwise distribution of the velocity was approximately uniform. Moreover, they found that in the far field the mean properties of the jet remained unchanged and turbulent energy was transferred to large scales thus indicating an inverse cascade characteristic of quasi-two-dimensional turbulence. Dracos *et al.* (1992) observed and studied the significance of large coherent eddy structures in the jet. However, using only point measurements, they could not provide a complete dynamical study of these structures. Recently, Shinnëeb, Bugg & Balachandar (2011) conducted a statistical analysis of large vortical structures in shallow water jets using particle image velocimetry. However, their layer thickness ($W \sim 5\text{--}15d$) was such that the flow evolution was inherently three-dimensional (albeit confined), and they did not focus on the far field region since their measurements were taken only up to $z/W \leq 16$. Their study was also uncorrelated in time, and so they were unable to identify the inherent time-dependence of the flow quantitatively.

We believe that a study of quasi-two-dimensional jets in the regime identified by Dracos *et al.* (1992) is necessary to assess the impact of the characteristic flow structures on the mixing, dispersion and diffusion of tracers in shallow jets, as suggested by Jirka (2001). For instance, undiluted patches of pollutants carried by a river discharging into the ocean can be disastrous for the local ecology. Information about the size, speed and typical travel distances of these patches is therefore crucial. To address this problem, we analyse the far field of a confined plane jet using particle image velocimetry. With a fully resolved velocity field in time and space we can characterise the jet structure phenomenologically. We are particularly interested in understanding quantitatively the relationship between the large-scale, and inevitably transient, flow structures and the long time-averaged mean properties of the plane jet.

The rest of this paper is organised as follows. In §2 we describe the experimental procedure. In §3 we then provide a qualitative overview of the flow structures observed from dyed jet experiments and instantaneous velocity fields, while in §4 we compare measurements of the time-averaged velocity field with classical theories for two-dimensional plane jets. In §5 we present a quantitative study of the flow structures, in particular by tracking the large eddies as they interact with the high-speed core. We discuss how the frequency of occurrence of the eddies changes with distance due to eddy merger. The study of the probability density function of the core shows that the time-averaged mean distribution of the velocity is due to the large-scale dynamics of the core and eddy structure. Finally in §6 we draw our conclusions.

2 Experimental procedure

The experimental apparatus is shown schematically in figure 1. Water jets were discharged vertically upward in a $1\text{ m}(L) \times 0.01\text{ m}(W) \times 1\text{ m}(H)$ tank made of 10 mm-thick Perspex sheets. An aluminium structure, made of two vertical beams located 0.4 m apart on each side of the jet axis and one horizontal beam located 0.8 m above the nozzle, was added on each side of the tank to increase the rigidity of the walls and ensure a uniform gap width. Two overflows on the side of the tank maintained a constant water depth at 0.915 m. The flow was driven by a constant-head tank and discharged via a 0.1 m circular rigid tube of aspect ratio 20 leading to a $5\text{ mm}(d) \times 10\text{ mm}(W) \times 20\text{ mm}$ chamber and finally into the tank. The aspect ratio of the tube was deemed sufficient to suppress any swirl in the flow. The flow rate was

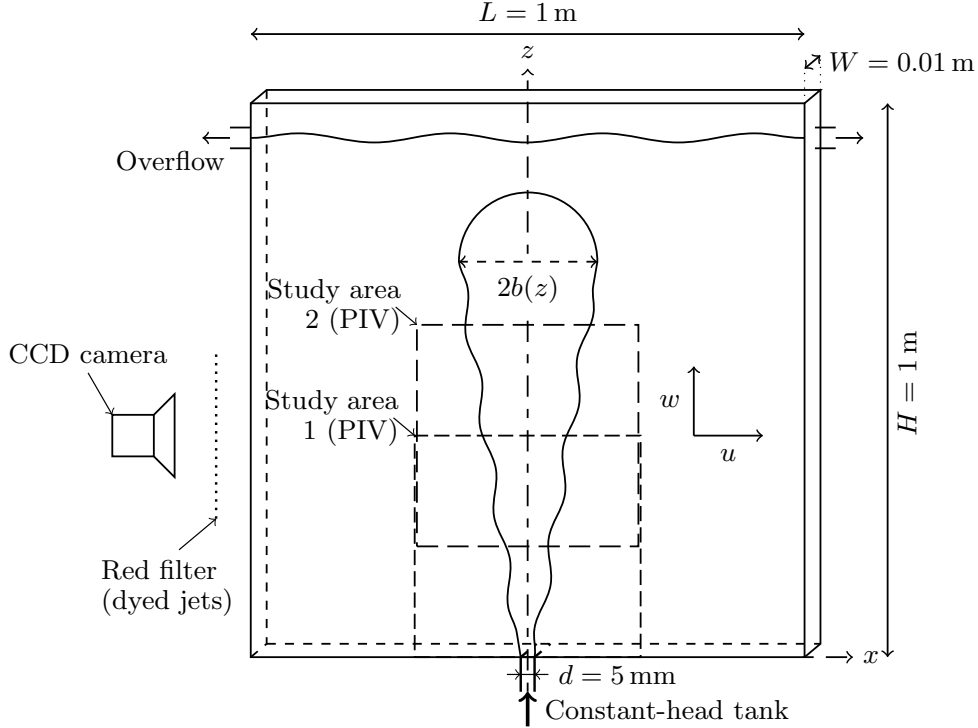


Figure 1: Schematic diagram of the experimental apparatus. The two PIV study areas are shown with overlapping dashed lines.

controlled through a valve and measured with a precision balance and a stopwatch for each experiment. The flow rate was found to be consistent in time with an accuracy of approximately 1%. We conducted two distinct sets of experiments using two qualitatively different techniques: dye tracking and particle image velocimetry (PIV).

2.1 Dye tracking experiments

For the dye tracking experiments, we filled the tank with fresh tap water. We injected dark blue food dye through a needle placed 0.2 m upstream of the nozzle. Simultaneously, we pumped the same volume of fluid out to minimise the disturbance introduced into the flow. Also, we injected the dye after the flow reached a steady state in the tank. We used diffuse ambient lighting for these experiments. A red filter was placed between the objective of the camera and the tank, as shown in figure 1, to increase the contrast between the jets and the background. The flow motion was recorded with a high-speed 8 bit grey-scale camera, Fastcam SA1.1 - Photron, mounted with a 62 mm focal-length lens. We analysed forty dyed jets with jet Reynolds number $2280 \leq Re_j = dw_s/\nu \leq 4030$, where w_s is the source velocity and ν is the kinematic viscosity of water, using the software code *DigiFlow* (Sveen & Dalziel, 2005). We determined the location of the edge of each dyed jet through an intensity criterion. Since the contrast

between the dyed surface and the background was very strong but not saturated, the edge of the jet was very sharp.

2.2 Particle image velocimetry experiments

For PIV experiments the tank was filled with water mixed with Pliolite VTAC particles of average diameter 0.23 mm, which served as passive fluid tracers for the PIV. Approximately 2 mL of rinsing agent (Finish® rinse aid) was added to the mixture to prevent aggregation of Pliolite particles. The small change in surface tension had no influence on the measurements. The choice of this particle size depended on both hydrodynamic and optical criteria (see for example Drayton, 1993). We find that the particle diameter is of the order of the smallest Kolmogorov length scale found in the flow, $\eta \approx 0.2$ mm. Although this size is not optimal to study small-scale turbulence, it was the minimum size that could be detected by the image software while also capturing the largest length scales in the flow. The particle Stokes number based on the Kolmogorov time scale was $St_{K} \leq 10^{-1}$ (see Xu & Bodenschatz, 2008), which guaranteed that these particles followed the fluid motion closely. The particle concentration was kept relatively uniform at approximately 1.7×10^{-5} by volume due to the turbulence in the tank. Since the particle concentration was smaller than 10^{-3} by volume then particle–particle interactions and any changes in the fluid viscosity were insignificant (see Fung, 1990, for more discussion). We adjusted the water density to match the particle density of 1.03 g cm^{-3} by adding 35 g of salt per litre of water. At rest, the particle distribution remained unchanged over 18 hours, thus confirming that the particles were neutrally buoyant. The mixture of salt water and particles recirculated in the experimental set-up in order to have identical conditions (particle concentration, water density and water temperature) for each experiment.

We performed the PIV experiments in a dark room. Two 1 kW filament photographic lamps, each mounted with a long focal-length spherical lens to focus the filament into a sheet, illuminated the tank from above through a 5 mm slit centred on the mid-plane ($y = 0$). Every effort was made to keep the width of the light sheet constant and smaller than the gap width in order to attenuate reflection issues with the tank walls. This also meant that we could not make any measurements away from the mid-plane ($y = 0$) because as we moved the light sheet closer to the wall in the narrow gap, reflection at the wall perturbed the measurements. From image inspection, the number of particles which appeared much slower than the rest, probably because they were trapped in the boundary layers, was sufficiently small (of the order of 10%) not to affect the imaging analysis and corrupt the computation of the velocity field. We recorded the flow motion using the same high-speed camera as described above. The camera filmed two $0.4 \text{ m} \times 0.4 \text{ m}$ study areas centred on the jet axis (as shown in figure 1). The frequency of image acquisition was set at 500 Hz for a duration of 10.9 s for study area 1 and 250 Hz for a duration of 21.8 s for study area 2. The acquisition frequency was much higher than the largest Kolmogorov frequency scale. Moreover, the length of the video was long enough to compute meaningful temporal averages. Study area 1 covered a height from $z = 0$ –0.4 m, while study area 2 covered a height from $z = 0.2$ –0.6 m. Hence, the jet was studied from its source up to a distance of $120d$. The width of the study area is larger than the length scale of the jet at every height. The 1024×1024 pixel images were analysed using *DigiFlow* (see Sveen & Dalziel, 2005, and references for more detail about the PIV algorithm used by *DigiFlow*). The spatial velocity resolution was at 6.6 mm based on interrogation areas of 17×17 pixels with 75% overlapping. This resolution proved to be sufficiently small from $z = 20d$ upward. Six steady turbulent jets of flow rates 33.2, 37.0 and $40.3 \text{ cm}^3 \text{ s}^{-1}$ were investigated in both study areas. The jet Reynolds number ranged from $3320 \leq Re_j \leq 4030$.

3 Qualitative observations

A sequence of grey-scale pictures of a typical injection of dye in a steady-state jet with $Re_j = 3850$ is presented in figure 2 as the dye front rises through the full depth of the quasi-two-dimensional tank. These pictures reveal many interesting features of quasi-two-dimensional jets. The saturated dye clearly shows the maximum lateral extent of the turbulent jet. The dye gradually fills a triangle (plotted in black lines) which suggests that entrainment is self-similar with height, at least when averaged over sufficiently long times. Before filling the full triangle width, we can observe (especially in figures 2*d* and 2*e*) an oscillation of the jet, as the dye path is clearly sinuous. Large round structures corresponding to eddies can also be identified on either side of the centreline. Dracos *et al.* (1992) observed similar structures for a range of distances $10 \leq z/W \leq 120$. The curvy edge of the jet suggests a characteristic scale, typically half the width of the triangle (approximately 10 cm at mid-height). These eddies result from the instability of the shear layer at the border between the jet and the ambient fluid (Jirka, 2001). Furthermore, tongues of ambient fluid (in white or light grey) appear at the rear of the largest eddies (see arrow in figure 2*e*). This phenomenon was also observed by Dimotakis, Miake-Lye & Papantoniou (1983) in the far field of round turbulent jets, and by Thomas & Brehob (1986) for two-dimensional turbulent jets. The role played by the eddies in the entrainment, by means of engulfment mechanisms at their rear, was modelled by De Young (1997) in an attempt to determine quantitatively the mass inflow contribution of large-scale structures in two-dimensional mixing layers.

Although the eddies observed in quasi-two-dimensional jets, such as the jet presented in figure 2, have some similarities with eddies in planar two-dimensional jets, it is important to note that the latter are genuine three-dimensional eddies while the former should be referred to as quasi-two-dimensional eddies because of the restriction imposed on the flow in the spanwise direction. The growth dynamics of quasi-two-dimensional eddies is governed by an inverse cascade of turbulence, while three-dimensional eddies tend to grow with mean-flow length scales. On the other hand, quasi-two-dimensional eddies also differ from purely two-dimensional eddies because friction at the boundaries, although relatively weak, restrains the maximum size of the eddies (Jirka, 2001) and eventually leads to their disintegration (Dracos *et al.*, 1992). Finally, it is worth noting that at the leading edge the dye concentration attenuates suggesting that diffusion occurs in a steady jet. Diffusion in quasi-two-dimensional jets is likely to be the result of a complex interaction between the eddies and the sinuous turbulent core of the jet.

The second batch of experiments involved quantitative measurements of the velocity field using PIV technique. Typical results for a jet at Reynolds number 4030 analysed in study area 2 are depicted in figure 3. In figure 3(*a*), a superposition of 40 images of the filming of the experiment shows the tracers as streaks to help visualise Eulerian structures in the flow. The corresponding velocity field is presented in figure 3(*b*), and it is clear that the main structures of the jet have been captured by the PIV. A high-speed core undulates along the centreline and is bordered by alternating counter-rotating eddies on the sides. The eddies are responsible for the entrainment and detrainment of fluid to and from the central core in a time-dependent fashion. Due to the particular geometry of the tank, the turbulence cannot develop isotropically and we observe rather an inverse turbulent cascade in which quasi-two-dimensional eddies grow with height (De Young, 1997). This mechanism is confirmed in the experiment, as flow structures increase in size as they are advected upward. The schematic cartoon displayed in figure 3(*c*) summarises these ideas. The time-averaged mean picture of quasi-two-dimensional jets is associated with a triangular shape encapsulating all the flow structures while the time-dependent picture shows a sinuous core flanked by large growing eddies. This two-part structure remains self-similar with height and its dynamics is responsible for the Gaussian distribution of the mean velocity as we will discuss in §5.

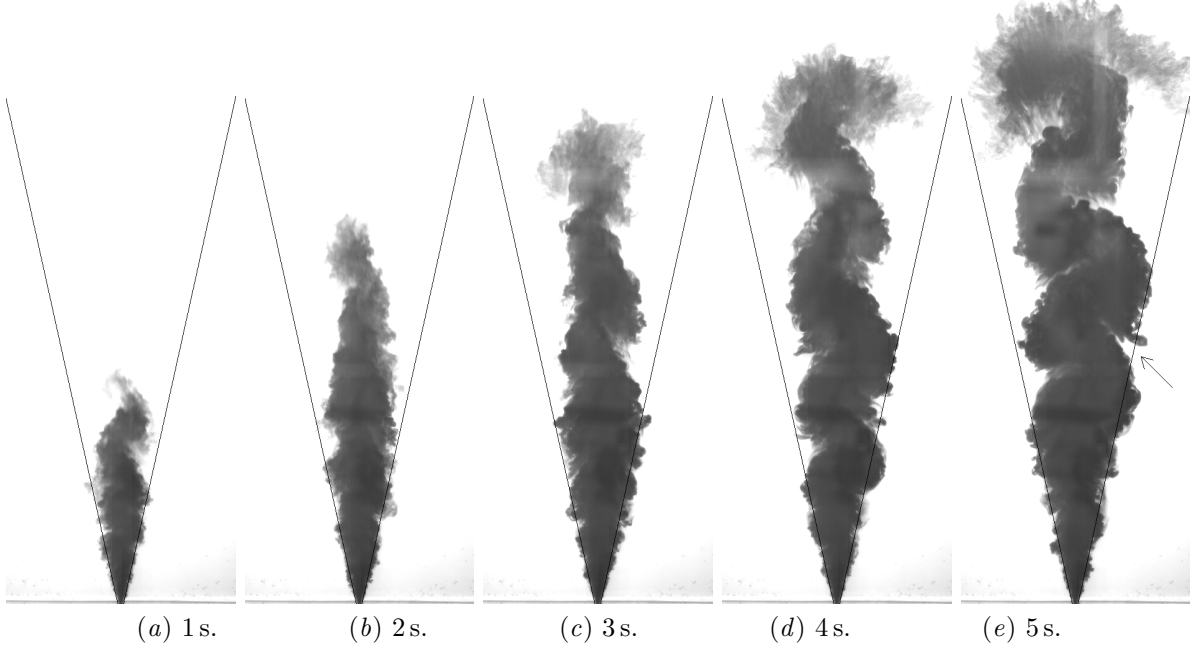


Figure 2: Sequence of grey-scale pictures of a dyed jet ($Re_j = 3850$) rising in the tank. The average dye edge is plotted with black lines. The arrow in figure 2(e) points at the engulfment mechanism occurring at the rear of an eddy.

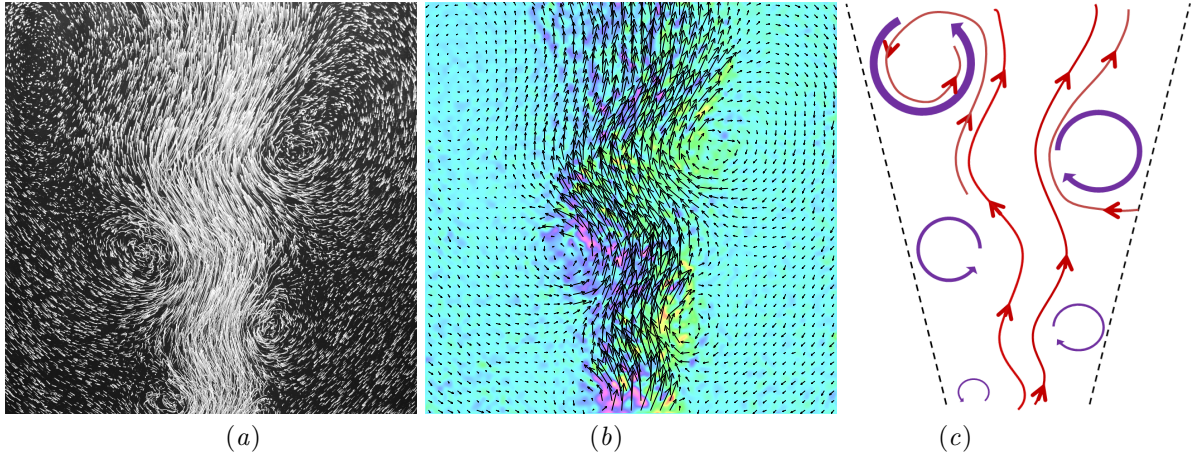


Figure 3: (a) Passive tracers (Pliolite particles) shown as streaks in a typical jet ($Re_j = 4030$) filmed in study area 2. (b) Velocity field (arrows) and vorticity field (background) of the same jet. (c) Schematic diagram describing the structure of two-dimensional jets.

4 Time-averaged mean flow field

To characterise the mean behaviour of quasi-two-dimensional jets, we consider the ideal model of a turbulent momentum jet in a two-dimensional semi-infinite environment. Adopting the same conventions as Jirka & Harleman (1979), the flow is considered incompressible and steady in the mean. The x -direction is the lateral, cross-jet direction, the y -direction is the spanwise direction and the z -direction is the streamwise, axial direction. The velocity components are designated by (u, v, w) for the Cartesian system (x, y, z) with the origin at the nozzle exit. We assume a plane flow in the domain: the velocity field and any other quantities are invariant with y , and $v = 0$ everywhere. This hypothesis can be justified in three ways: the velocity profile across the gap must be self-similar in the core and the influence of the boundary layers is of second order at high Reynolds number; the v -component of the velocity is negligible compared to the other two components; and ambient fluid can only be entrained from the sides of the jet, i.e. in the x -direction. We also use the common hypothesis of a Gaussian profile (see, for instance, List, 1982) for the time-averaged vertical velocity:

$$\overline{w}(x, z) = \overline{w}_m(z) \exp \left[- \left(\frac{x}{b(z)} \right)^2 \right], \quad (1)$$

where the over-bar represents an appropriate average in time, $w_m(z)$ is the maximum vertical velocity at distance z from the source and $b(z)$ is a measure of the local lateral spread of the jet velocity. We derive briefly the governing equations for plane jets, based upon the conservation of volume and momentum (see, for instance, Kotsovinos & List, 1977, for more details). The time-averaged volume flux and the time-averaged momentum flux are expressed respectively as

$$\overline{Q}(z) = \int_{-\infty}^{\infty} \overline{w}(x, z) dx \quad \text{and} \quad \overline{M}(z) = \int_{-\infty}^{\infty} (\overline{w})^2(x, z) dx. \quad (2a, b)$$

Solving the first-order integrated equations of motions, we find

$$\frac{d\overline{M}}{dz} = 0, \quad \frac{d\overline{Q}}{dz} = 2\alpha\overline{w}_m \quad \Rightarrow \quad \overline{M} = M_0, \quad \overline{Q} = Q_0 \left(4\sqrt{2}\alpha \frac{M_0 z}{Q_0^2} + 1 \right)^{1/2}, \quad (3a-d)$$

where we assume in (3b) that the entrainment velocity is proportional to the maximum time-averaged vertical velocity, with α the entrainment coefficient (Morton, Taylor & Turner, 1956), and Q_0 and M_0 are values at the origin for the volume flux and momentum flux respectively. The e-folding value of the maximum time-averaged vertical velocity and the maximum time-averaged vertical velocity are respectively

$$b(z) = \frac{Q_0^2}{\sqrt{2\pi}M_0} \left(4\sqrt{2}\alpha \frac{M_0 z}{Q_0^2} + 1 \right) \quad \text{and} \quad \overline{w}_m(z) = \frac{\sqrt{2}M_0}{Q_0} \left(4\sqrt{2}\alpha \frac{M_0 z}{Q_0^2} + 1 \right)^{-1/2}. \quad (4a, b)$$

We can infer the theoretical virtual origin of the jet $z_0 = -Q_0^2/(4\sqrt{2}\alpha M_0)$, which results from the choice of the boundary conditions (i.e. the distributions of the volume flux and momentum flux at $z = 0$).

Alternatively, solving the plane jet equations assuming momentum-flux conservation and similarity (see, for example, Pope, 2000), also leads to the same power laws for the e-folding value of the maximum time-averaged vertical velocity, $b \propto (z - z_0)$, and the maximum time-averaged streamwise velocity, $\overline{w}_m \propto$

$(z - z_0)^{-1/2}$. The constants of proportionality and the virtual origin can differ because of the assumptions we make for the x -distribution of \bar{w}_m (essentially due to ‘shape factors’) and for the boundary conditions. As a direct comparison with the ‘velocity spread rate’ S defined as $dx_{\frac{1}{2}}/dz = S$ (where $x_{\frac{1}{2}}$ is the velocity half-width defined by $\bar{w}_m(z)/2 \equiv \bar{w}(x_{\frac{1}{2}}, z)$) we can remark that $S = 4(\ln 2/\pi)^{1/2}\alpha$ (see Pope, 2000, for further details about S).

Equations (4a,b) suggest that the natural scalings for length and time scales in our problem are d , the source width, and $\tau = d^2/Q_0$ respectively. Therefore when considering our experimental data we will always scale quantities with these scalings, i.e.

$$\hat{z} = \frac{z}{d}, \quad \hat{x} = \frac{x}{d}, \quad \hat{b} = \frac{b}{d}, \quad \hat{t} = \frac{t}{\tau}, \quad \hat{w} = \frac{\tau}{d}w, \quad (5)$$

where hats denote non-dimensional variables.

For comparison with the theoretical model we time-averaged the velocity field measured with PIV. We plot the lateral spread, the evolution with height and the horizontal distribution of the time-averaged vertical velocity. We also discuss the influence of the free surface at the top boundary, the impact of the lateral confinement and possible three-dimensional effects on the flow, such as friction at the walls constraining the flow.

In figure 4, we show the ensemble average of the edges of 40 dyed jets (plotted with dots). The evolution of the dye edge with height clearly indicates that above $z/d = 120$ the influence of the free surface becomes non-negligible. This height serves as a lower bound for the ‘impingement region’ (see Jirka & Harleman, 1979, for a detailed study). The zone of established flow is found to start at approximately $z/d = 20$, a value at which the vertical velocity becomes self-similar. This value is commonly reported in the literature (see for example Kuang, Hsu & Qiu, 2001). A linear fit of the non-dimensional average dye edge (plotted with a thin line in figure 4) calculated between $20 \leq z/d \leq 120$ gives a slope of 0.22 ± 0.08 for the half-spreading angle. We can observe that the non-dimensional e-folding value of the maximum time-averaged vertical velocity \hat{b} (plotted with crosses), is much narrower. We discuss this difference further below. We also compute the quantity \hat{b} from the ensemble average of the 12 jets studied with PIV. A linear fit (plotted with a thick line) calculated between $20 \leq z/d \leq 120$ gives the rate of change: $db/dz = 0.154 \pm 0.016$, which is slightly above the value of 0.135 reported by Ramaprian & Chandrasekhara (1985) and very similar to the value based upon Albertson *et al.* (1950). Using (4a) the corresponding entrainment coefficient (determined to best-fit the vertical variation of b) is $\alpha_b = 0.068 \pm 0.007$ (which is equivalent to $S_b = 0.125 \pm 0.015$), and we find that α_b is almost constant in the zone of established flow, thus confirming the entrainment assumption (Morton *et al.*, 1956).

In figure 5, we plot the non-dimensional maximum time-averaged vertical velocity $\bar{w}_m/(Q_0/d)$ against height. The crosses are plots of an ensemble average over all the jets studied with PIV. Although the agreement is good, they lie slightly but systematically above the theoretical curve (plotted with a solid line) for $z/d \leq 100$. We computed the theoretical curve from (4b) and using $\alpha = \alpha_b$. Q_0 was measured for each jet as described in the experimental procedure. On the other hand, since M_0 could not be measured directly it was replaced by \bar{M} by virtue of (3c). As shown in figure 6, the momentum flux \bar{M} (plotted with pluses) computed from the time-averaged vertical velocity field using (2b) (the boundaries of the integral are chosen as the positions where $\bar{w}_m = 0$) is found to be approximately constant for $34 \leq z/d \leq 110$. For $z/d < 34$, the data do not seem accurate probably because the frame rate is not high enough for the large velocity at that distance and the resolution of the PIV could also not be optimal where the jet is very narrow. For $z/d > 110$, the influence of the impingement region as the jet approaches the

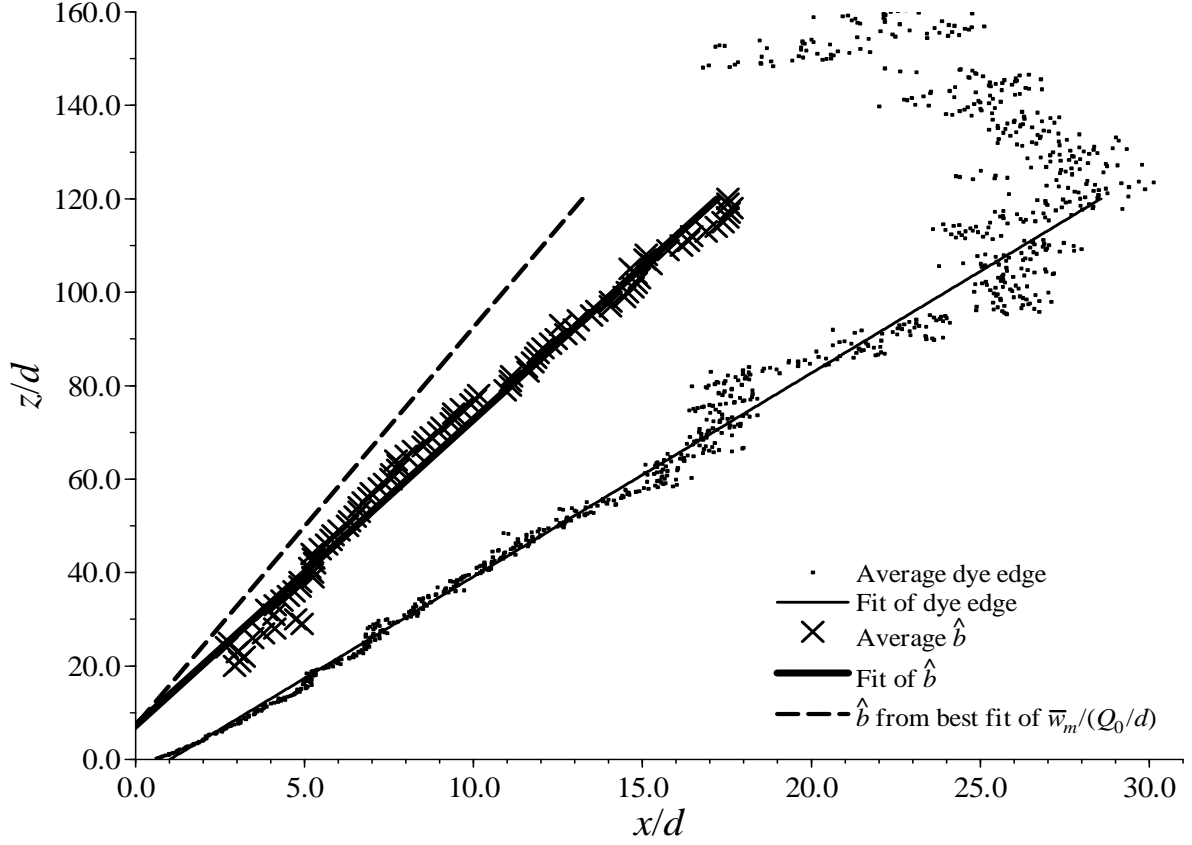


Figure 4: Non-dimensional average dye edge (plotted with dots) with a linear fit (plotted with a thin line) and non-dimensional e-folding value of the maximum time-averaged vertical velocity \hat{b} (plotted with crosses) with a linear fit (plotted with a thick line). Non-dimensional average velocity spread rate (plotted with a dashed line) using $\alpha = \alpha_{\bar{w}_m}$ computed from the best fit of $\bar{w}_m/(Q_0/d)$ (see figure 5).

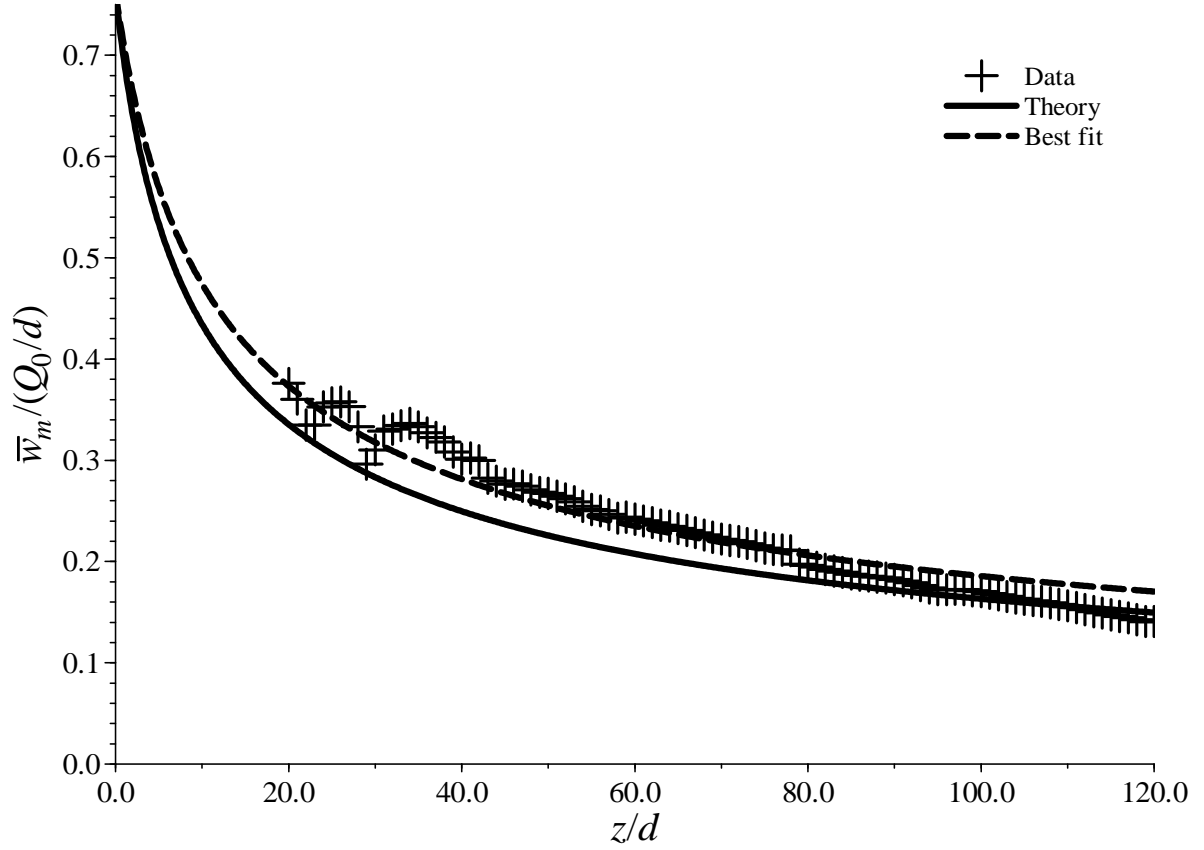


Figure 5: Non-dimensional maximum time-averaged vertical velocity (plotted with pluses) versus height, theoretical curve (plotted with a solid line and using $\alpha_b = 0.068$) and best least square fit (plotted with a dashed line) optimising with respect to α (using $\alpha_{\bar{w}_m} = 0.052$).

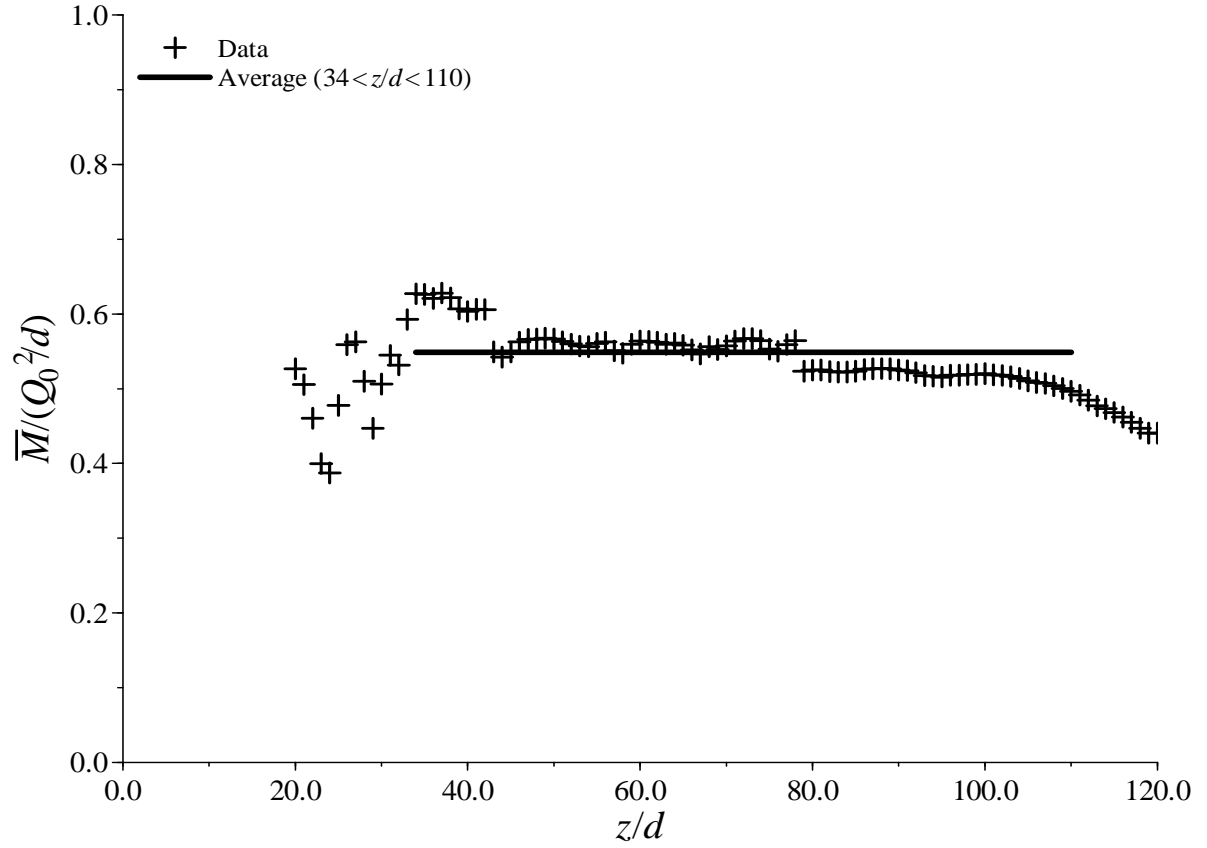


Figure 6: Non-dimensional time-averaged momentum flux (plotted with pluses) versus height and average value $\langle \bar{M} \rangle / (Q_0^2/d) = 0.55$ (plotted with a solid line).

free surface at the top seems to start affecting the momentum flux. The mean non-dimensional value of the momentum flux is $\langle \overline{M} \rangle / (Q_0^2/d) = 0.55 \pm 0.03$ (plotted with a solid line in figure 6). Giger *et al.* (1991) reported and discussed the wide range of values for the non-dimensional momentum flux measured in plane jets from the literature: from 0.52 (Cervantes de Gortari & Goldschmidt, 1981) to 1.77 (Antonia, Satyaprakash & Hussain, 1980). We analysed the influence of friction at the rigid boundaries on the momentum flux and found a Fanning friction factor of $f \approx 0.007$ assuming a wall stress of the form $\tau_w = f\rho \langle \overline{w} \rangle^2 / 2$, where ρ is the water density and $\langle \overline{w} \rangle$ is the spatial-averaged velocity in the y -direction (Bird, Stewart & Lightfoot, 2007). The influence of friction is relatively small compared to the mean value of the momentum flux (of the order of 10%) and therefore has not been included in our constant momentum-flux model (see Giger *et al.*, 1991, for a detailed study). In figure 5, a least square fit of the data (plotted with a dashed line) assuming equation (4b) and optimising with respect to the entrainment coefficient yields an optimal choice for α from the z -dependence of the maximum velocity $\alpha \overline{w}_m = 0.052$ (which is equivalent to a velocity spread rate $S_{\overline{w}_m} = 0.098$). The fact that $\alpha \overline{w}_m$ (also plotted with a dashed line in figure 4) is slightly smaller than α_b means that some assumptions of the model underlying (4)a and b (which should yield identical estimates for α using $b(z)$ and $\overline{w}_m(z)$) are not perfect. In particular, we believe that the Gaussian distribution hypothesis is not ideal, as slight deviations from Gaussianity could explain the mismatch.

In figure 7(a), we show the horizontal distribution of the normalised time-averaged vertical velocity $\overline{w}/\overline{w}_m$. The horizontal axis is centred on the position of the maximum time-averaged vertical velocity. All the curves result from an ensemble average of 6 or 12 jets, depending where the vertical position of the curve lies with respect to the two study areas for the PIV. The experimental data (plotted with different colours) are in very good agreement with the theoretical curve (plotted with a thick red line) computed from equation (1) using $\alpha = \alpha_b$ and neglecting any consideration of virtual origin (Kotsovinos, 1976). Nevertheless, the experimental curves are somewhat narrower than the theoretical Gaussian velocity profile. This discrepancy is consistent with a smaller entrainment coefficient, as suggested by the best fit of $\overline{w}_m/(Q_0/d)$ in figure 5. The mismatch is probably caused by the return flow in the tank which is not accounted for by the model where an infinitely wide domain is assumed.

The problem of the return flow in a finite-lateral-extent domain is more prominent in plane jets than in (fully unconfined non-planar) three-dimensional jets. In plane jets, the entrainment velocity remains constant outside the jet whereas it decreases with distance in the three-dimensional case. As a consequence, we can observe a negative shift in the horizontal distribution of the time-averaged vertical velocity (see figure 7a), which denotes the presence of the return flow. The flux of the return flow, \overline{Q}_r , increases with height as it matches exactly the jet volume flux \overline{Q} due to conservation of volume at every height across the width of the tank. We can estimate the time-averaged vertical velocity distribution of the return flow by applying volume conservation at each height. For all z , the total volume flux on both sides of the jet is $\overline{Q}_r = \overline{Q} - Q_0$. We assume that the return velocity is distributed uniformly along $-L/2 \leq x \leq -x_0$ and $x_0 \leq x \leq L/2$, where $x_0 \approx 0.25z$ is defined as the location where $\overline{w} = 0$. Therefore, using equations (3d) and (4b) we find that the time-averaged return velocity is

$$\frac{\overline{w}_r}{\overline{w}_m} = -\frac{Q_0^2}{2\sqrt{2}M_0(L/2 - x_0)} \left[\left(4\sqrt{2}\alpha \frac{M_0}{Q_0^2} z + 1 \right) - \left(4\sqrt{2}\alpha \frac{M_0}{Q_0^2} z + 1 \right)^{1/2} \right], \quad (6)$$

where we use $\alpha = \alpha_b = 0.068$ and $M_0 = \langle \overline{M} \rangle = 0.55 Q_0^2/d$ to plot figure 7(b). As can be seen in figure 7(b), adding this simple estimation of the return-flow velocity \overline{w}_r to the jet velocity \overline{w} has corrected the negative shift in the experimental data. At every height, except $z/d = 20$, the velocity

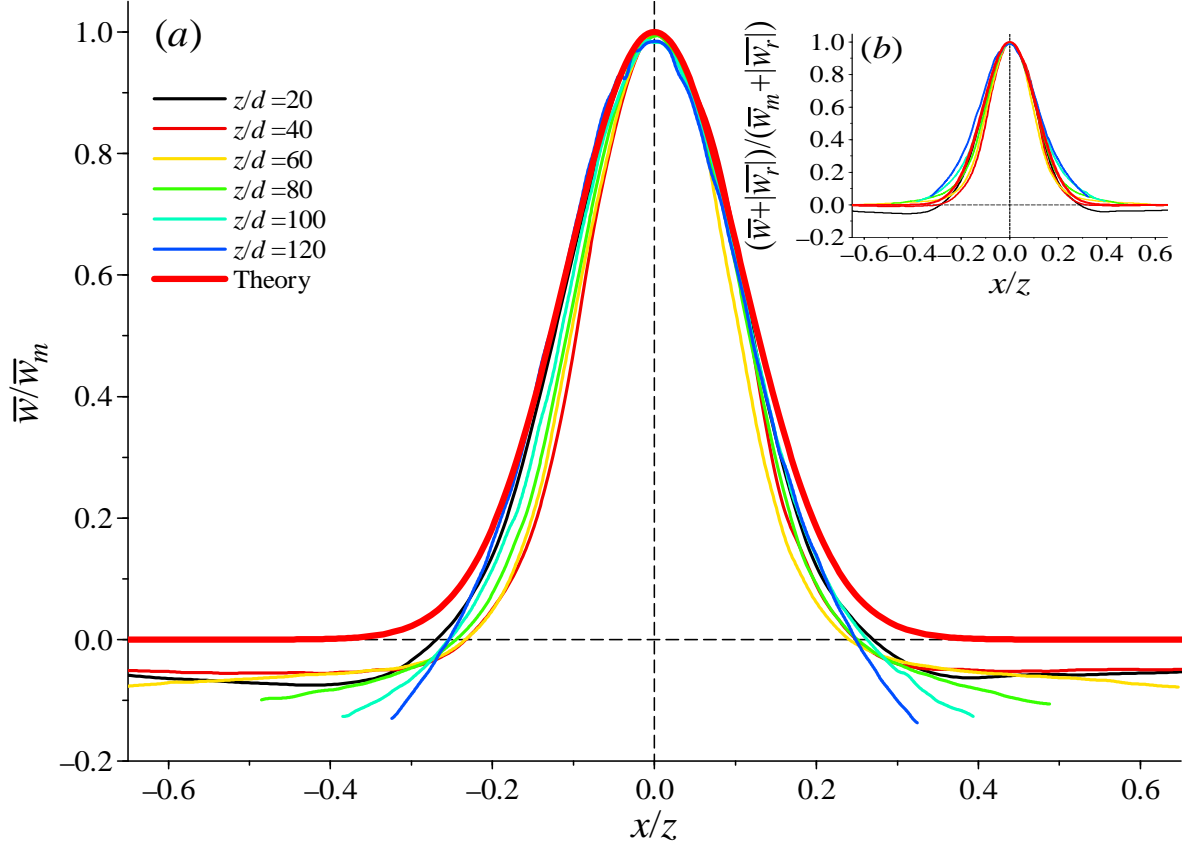


Figure 7: (a) Horizontal distribution of the normalised time-averaged vertical velocity at various heights (plotted with different colours) and theoretical prediction (plotted with a thick red line). (b) Horizontal distribution of the normalised sum of the time-averaged vertical velocity and the absolute value of the estimated time-averaged vertical velocity of the return flow (defined by equation 6) at the same heights as in (a) (plotted with different colours) and theoretical prediction (plotted with a thick red line).

tends to a zero asymptotic value for large $|x/z|$.

From comparison with similar experiments that we conducted in a smaller domain ($0.5 \text{ m} \times 0.01 \text{ m} \times 0.5 \text{ m}$) and with experimental results reported in the literature and obtained in larger tanks of various aspect ratios and with porous or non-porous lateral boundaries (Giger *et al.* (1991); Dracos *et al.* (1992); Rowland *et al.* (2009)), we believe that the impact of the return flow is limited and affects only the distribution of the time-averaged vertical velocity in the manner described above. From direct measurements we also find that the momentum flux associated with the return flow is small compared with the momentum flux in the jet (from 0 to 15% for $z/d = 0\text{--}110$). We have not observed any qualitative or quantitative influence of the return flow on the time-dependent core and eddy structure described in §3.

The experimentally measured vertical velocity field follows closely the predictions given by the derivation of the momentum and continuity equations for two-dimensional turbulent jets. The small difference due to the lateral confinement of the experimental jets leads us to the conclusion that the entrainment coefficient is within the range: $0.052 \leq \alpha \leq 0.068$. The purpose of the study of the mean flow is not to understand all the details of this flow but rather to give us some insight about the flow field in this particular geometry. More refined models for the plane jet can be found in the literature (see for example Giger *et al.*, 1991; Hussein *et al.*, 1994; Wang & Law, 2002).

5 Quantitative analysis of the time-dependent core and eddy structure

5.1 Time-dependent eddy structure

We now analyse the core and eddy structure of the flow using the experimental results given by the PIV. We identify large vortical structures or ‘eddies’ in individual frames of the instantaneous velocity field using *DigiFlow*, as shown in figure 8(a). Considering a specific frame, we find regions of the instantaneous flow field where streamlines form a complete loop. This technique is similar to the eddy identification method proposed by Robinson (1991). We plot the streamlines forming a complete loop in figure 8(a) with grey curves. We then analyse each patch, or eddy, to obtain statistical measurements such as the centroid (identified by the location of the black crosses) and the standard deviations in the horizontal and vertical directions (shown by the size of the crosses). The coordinates of the centroid $(x_{c,k}, z_{c,k})(t)$ of eddy ‘ k ’ at time t are computed numerically as

$$(x_{c,k}, z_{c,k})(t) = \frac{1}{\sum_{x=0}^{L_x} \sum_{z=0}^{L_z} \Delta_k(x, z, t)} \sum_{x=0}^{L_x} \sum_{z=0}^{L_z} (x, z)(t) \Delta_k(x, z, t), \quad (7)$$

where L_x and L_z are the horizontal and vertical dimensions of the velocity field and $\Delta_k(x, z, t)$ is 1 if the point $(x, z)(t)$ belongs to a streamline identified as part of eddy k at time t and 0 otherwise. Similarly, the horizontal and vertical standard deviations $(x_{s,k}, z_{s,k})(t)$ of eddy k at time t are computed numerically as

$$(x_{s,k}, z_{s,k})(t) = \left(\frac{1}{\sum_{x=0}^{L_x} \sum_{z=0}^{L_z} \Delta_k(x, z, t)} \sum_{x=0}^{L_x} \sum_{z=0}^{L_z} ((x, z)(t) - (x_{c,k}, z_{c,k})(t))^2 \Delta_k(x, z, t) \right)^{1/2}, \quad (8)$$

We applied the algorithm every ten frames to the six experimental velocity fields. The eddies are thus tracked in time at a frequency of 25 Hz. As a quality control of the technique, we conducted a visual

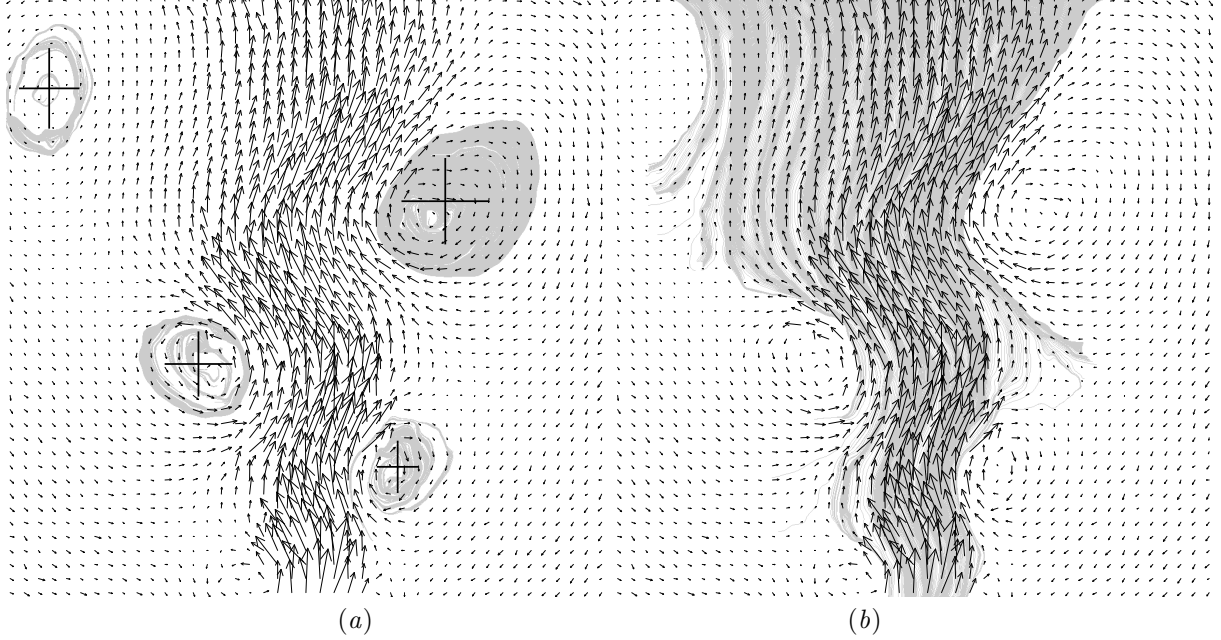


Figure 8: (a) Identification of the vortical structures in the instantaneous velocity field (plotted with black arrows). The streamlines identified within an eddy are plotted with grey curves. The black crosses designate the centroid of the eddies and the size of the crosses represents their standard deviations in the horizontal and vertical directions. (b) Identification of the core structure in the same instantaneous velocity field (plotted with black arrows). The streamlines identified as part of the core structure are plotted with grey curves.

inspection of all the eddies identified by the algorithm. This showed that the algorithm was very robust. It did not appear to be subject to ‘false positives’, i.e. the misidentification of a non-eddy feature of the flow as an eddy. The algorithm only occasionally failed to detect eddies (i.e. there were very few ‘false negatives’) when the eddies partially appeared at the edges of the frame.

The trajectories of 48 eddies are shown in figure 9 (plotted with black dots). A linear fit (shown with a solid line) gives an average slope of 0.22 from the vertical. We also plot the linear fits of the ensemble-averaged horizontal standard deviation of the eddies, a measure of the average eddy width, with dashed lines. The horizontal and vertical standard deviations were found to be almost identical, showing that the eddies are close to circular in shape. They both have a linear trend increasing with height at a rate of 0.07.

The non-dimensional location of each eddy in time has been plotted in figure 10 with dots. We can see a general trend which follows the power law $\hat{z} \propto \hat{t}^{2/3}$ (plotted with a solid curve) derived from the maximum time-averaged vertical velocity formula (4b). The large scatter is due to the complex dynamics of individual eddies. We found that not all eddies travelled through the depth of the PIV window completely unperturbed. We observed merging of close successive eddies with the first eddy slowing down considerably, sometimes even halting, and the following eddy accelerating substantially.

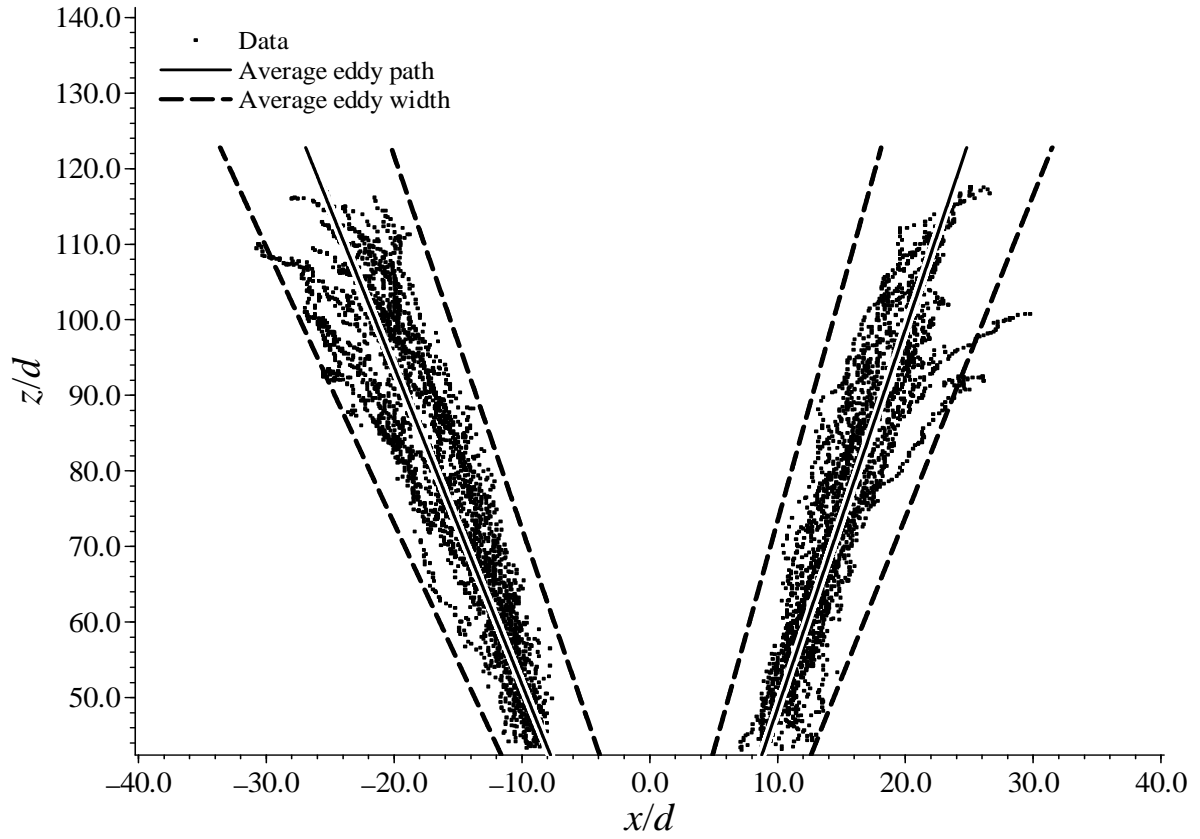


Figure 9: Eddy locations in PIV study area 2 (plotted with dots), linear fits of eddy locations (plotted with solid lines) and average eddy horizontal standard deviations (plotted with dashed lines).

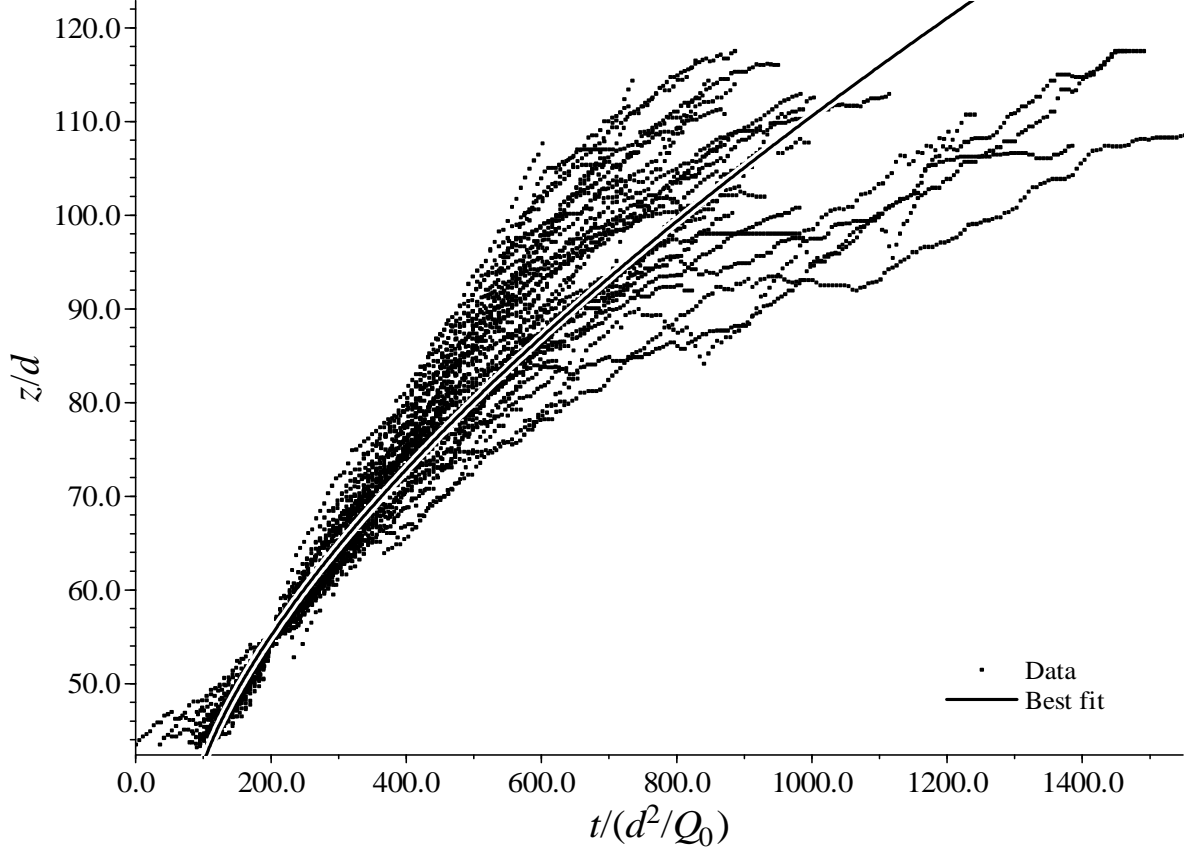


Figure 10: Eddy z -coordinate versus time (plotted with dots) and best least square fit (plotted with a solid curve) assuming $\hat{z} \propto \hat{t}^{2/3}$.

Similarly to Dracos *et al.* (1992)’s observations, we did not see eddies rotating around a common axis before merging. We also noticed some small eddies disappearing in the vicinity of the core. From the best fit of the eddy vertical position in time we find that the average eddy speed is 0.28 times the theoretical \bar{w}_m and 0.24 times the best fit of \bar{w}_m . The fastest identified eddy rises approximately at the same speed as the centreline time-averaged vertical velocity, whereas the slowest eddy rises at less than 15% of \bar{w}_m .

To investigate the eddy frequency, we counted the number of eddies (identified by the algorithm described above) passing at a given height on either side of the core of the jet. We measured this number for the 6 PIV experiments performed in study area 2 and then divided it by the duration of the experiment, i.e. 21.8 s. The resulting non-dimensional eddy frequency $\hat{f} = fd^2/Q_0$ is plotted with thin lines in figure 11(a). Dracos *et al.* (1992) found an empirical law for the eddy frequency, $\hat{f} = 176\hat{z}^{-3/2}$ (plotted in non-dimensional form with a dashed curve), and explained that f decreased due to the decrease

of the eddy transport velocity and due to merging mechanisms. However, if we assume that eddies form periodically then the eddy frequency should remain constant with height since eddies travel on average at the same velocity. The frequency can only decrease if eddies merge (or, to a lesser extent, disappear). Merging occurs when the distance between two successive eddies is smaller than a critical value. The distance between two eddies decreases because their transport velocity decreases like $\hat{z}^{-1/2}$ and because eddies grow approximately linearly with height due to entrainment of ambient fluid.

The punctuated decrease in frequency can actually be observed in figure 11(a) as we follow individual experiments (see the values of f for a typical experiment plotted with red crosses). The frequency f is constant over a certain distance and then drops by a discrete value in a step-wise way. This is also clearly shown by the evolution of the Strouhal number, $St = fb/\overline{w}_m$, plotted with dots in figure 11(b) and with red crosses for the same typical experiment. The Strouhal number increases like $St \propto \hat{z}^{3/2}$ from a minimum value of $St = 0.07$ consistent with the value reported by Dracos *et al.* (1992) (plotted with a dashed curve) and then drops, somewhat chaotically but consistently, to this minimum value as mergings occur. Because merging becomes less frequent as z/d increases, the length of time over which f is constant (and hence St increases) increases with z/d . This leads to the increase in both typical values of the Strouhal number and its variance, as is apparent in figure 11(b). The actual value of the minimum Strouhal number appears to depend on the eddy formation frequency, the travel speed of the eddies, the growth of the eddies due to entrainment and the dynamics of merging, in ways that are not as yet fully understood.

To summarise, the eddies have on average a linear trajectory, a constant growth with height and a velocity similar to the time-averaged mean vertical velocity of the jet. All these findings lead to the conclusion that the dynamics of the eddies is essentially self-similar with height, at least within the region of the flow which we have studied. From the analysis of the time evolution of the streamlines leading to the eddies, we can also attribute the growth of the eddies mainly to the entrainment of ambient flow. Eddy merging occurs irregularly and is responsible for the decrease of the long time-averaged eddy frequency, with an apparently well-defined minimum Strouhal number $St \geq 0.07$.

5.2 Time-dependent core structure

Similarly, we identify the core of the jet by plotting all the streamlines which exit through the top of a specific velocity field. Effectively, the algorithm follows the streamlines backward starting from the points at the top horizontal boundary of the velocity field. However, in the following discussion we consider the streamlines in the forward direction with their endpoint at the top of the velocity field. The identification of the streamlines of the core is repeated every ten frames for each PIV velocity field, thus giving a dynamical picture of the core at a frequency of 25 Hz. It can be seen in figure 8(b) that some streamlines (plotted with grey curves) start at the bottom boundary of the window while others come laterally inward. The streamlines coming from the bottom of the frame reveal the volume flux brought by the jet itself into the frame. The streamlines coming from the sides of the jet show the entrained volume flux. They actually reveal how entrainment of ambient fluid occurs as they wrap around eddies and then are incorporated into the core. It is clear that eddies constitute an essential entrainment mechanism by engulfing ambient fluid at their rear. The starting point of entrained streamlines (i.e. the location at which we consider them as part of the core) is chosen where the vertical component of their gradient changes sign.

This choice raises the more fundamental question about the boundaries of the core. The boundary between the core and the eddy is clearly defined since the algorithms used to identify both structures

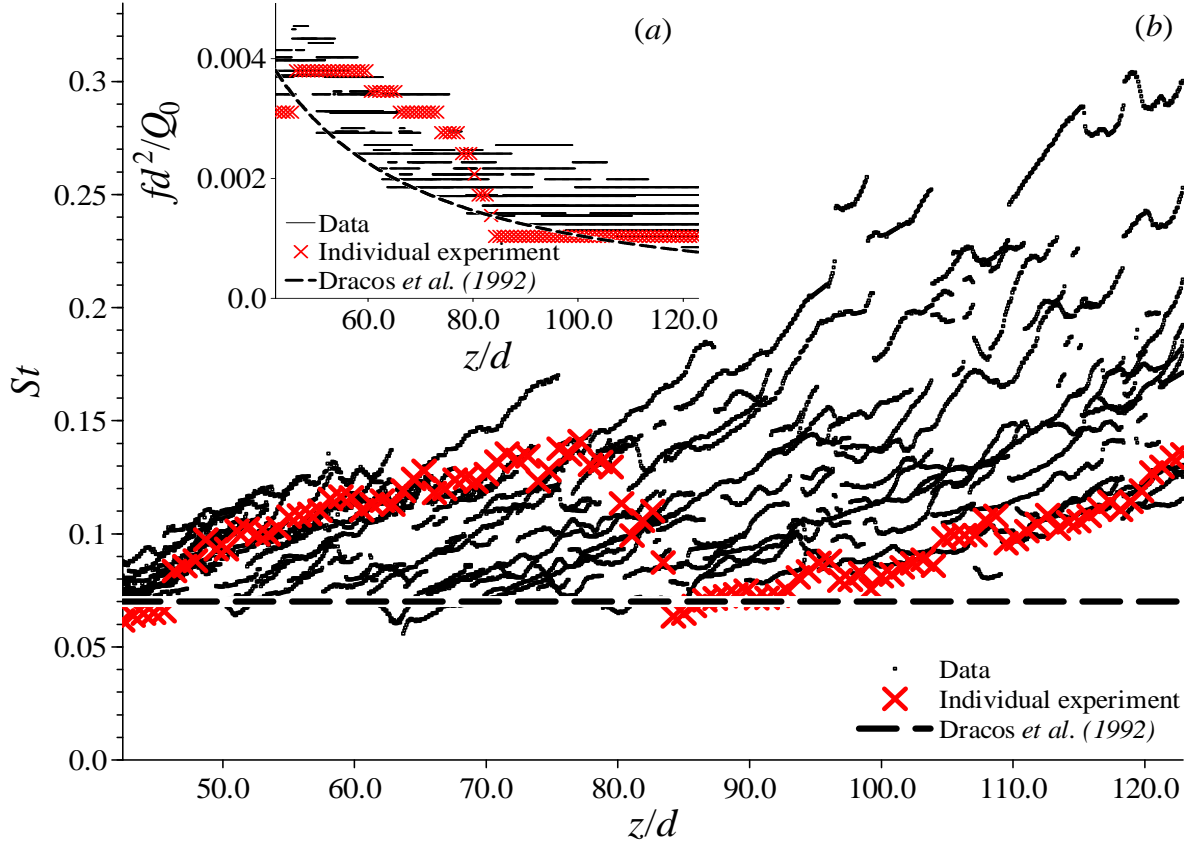


Figure 11: (a) Data for the non-dimensional eddy frequency fd^2/Q_0 versus height (plotted with thin lines) and best fit of Dracos *et al.* (1992) (plotted with a dashed curve). The values of fd^2/Q_0 for a typical individual experiment have been highlighted with red crosses. (b) Data for the Strouhal number $St = fb/\bar{w}_m$ versus height (plotted with dots) and Strouhal number reported by Dracos *et al.* (1992) (plotted with a dashed line). The values of St for the same experiment have also been highlighted with red crosses.

ensure mutual exclusion. However, at the top and bottom of the window this boundary can be ambiguous if large eddies are not entirely seen in the image frame. At the top of the frame the error zone is actually restricted to $z > 118d$, which is approximately where the self-similarity region of the jet ends. At the bottom of the frame the error zone is insignificant since the eddies are much smaller. Moreover, we found that the starting point chosen for entrained streamlines has no effect on the time-averaged distribution of the core and negligible impact on time-dependent distributions. Therefore, although somewhat arbitrary, we believe that our criterion determining the boundary between the core and the ambient flow reflects the diffusion of momentum from the jet to the ambient flow.

We present the distribution of the probability density function (PDF) of the core (plotted with thick solid curves) at different heights in figure 12. The discrete formulation of the PDF is

$$PDF(x, z) = \frac{1}{N} \sum_{n=0}^N \Delta_n(x, z), \quad (9)$$

where N is the total number of frames for a given experiment, n designates the n^{th} frame and $\Delta_n(x, z)$ is 1 if the point (x, z) belongs to a streamline identified as part of the core of the jet and 0 otherwise. Its shape is Gaussian-like on the edges and flatter in the middle. The flat portion corresponds to the section of the jet always occupied by the core. The width of this section grows linearly with height on average, as shown by the standard deviation measurement $\overline{x_{std}}$ (plotted with thin solid curves for the experimental data and dashed lines for the linear fits), at a rate of 0.12. Furthermore, the momentum flux of this portion remains constant with height at a value of 78% of the total momentum of the jet. The edges of the PDF correspond to the lateral excursions of the core. It is interesting to note a similarity between the distribution of the PDF of the core, as presented in figure 12, and a typical distribution of the intermittency function measured in quasi-two-dimensional jets (see, for example, Dracos *et al.*, 1992). Both display a plateau equal to one in the interior of the jet and a Gaussian-like decrease tending towards zero as $|x/z|$ increases. Nevertheless, the intermittency function and the PDF of the core are different both in the way they are computed and in their meaning. The PDF of the core is a measure of the probability of being in the core (which is identified by the algorithm described above). On the other hand, the intermittency criterion measures the probability of being in a turbulent region. The similarity observed between these two functions is probably due to the fact that the core is a region where the amplitude of the turbulent fluctuations increases toward the jet centreline. However, the lateral spreading of the two functions should differ because, contrary to the intermittency function, the PDF of the core excludes the eddies, which are also regions of large velocity fluctuations.

A typical standard deviation $x_{std}(t)$ of the PDF of the core at the time instant corresponding to the jet shown in figure 8(b) is plotted with dashed curves in figure 13. The undulations of the jet, which we already observed on dyed jet pictures, are primarily a feature of the edges of the core. The distribution of the instantaneous vertical velocity $w(t)$ corresponding to the same time instant is plotted with solid curves at different heights in figure 13. We normalise $w(t)$ with the maximum instantaneous vertical velocity w_n measured at the lowest height in the frame, $\hat{z}_n = 42.4$. We can observe that the instantaneous velocity decreases with height and spreads laterally as expected from the self-similar theoretical model. Furthermore, the velocity distribution is not centred on the z -axis but follows the undulations of the core described by $x_{std}(t)$. The velocity within the core is much larger than the velocity outside, thus underlying the presence of this high-speed core in the jet. It is also very interesting to note that the lateral decrease of the velocity is slower in the interiors of the undulations than in the exteriors. It is due to the presence of the eddies (shown as crosses, with the size of the crosses representing the horizontal

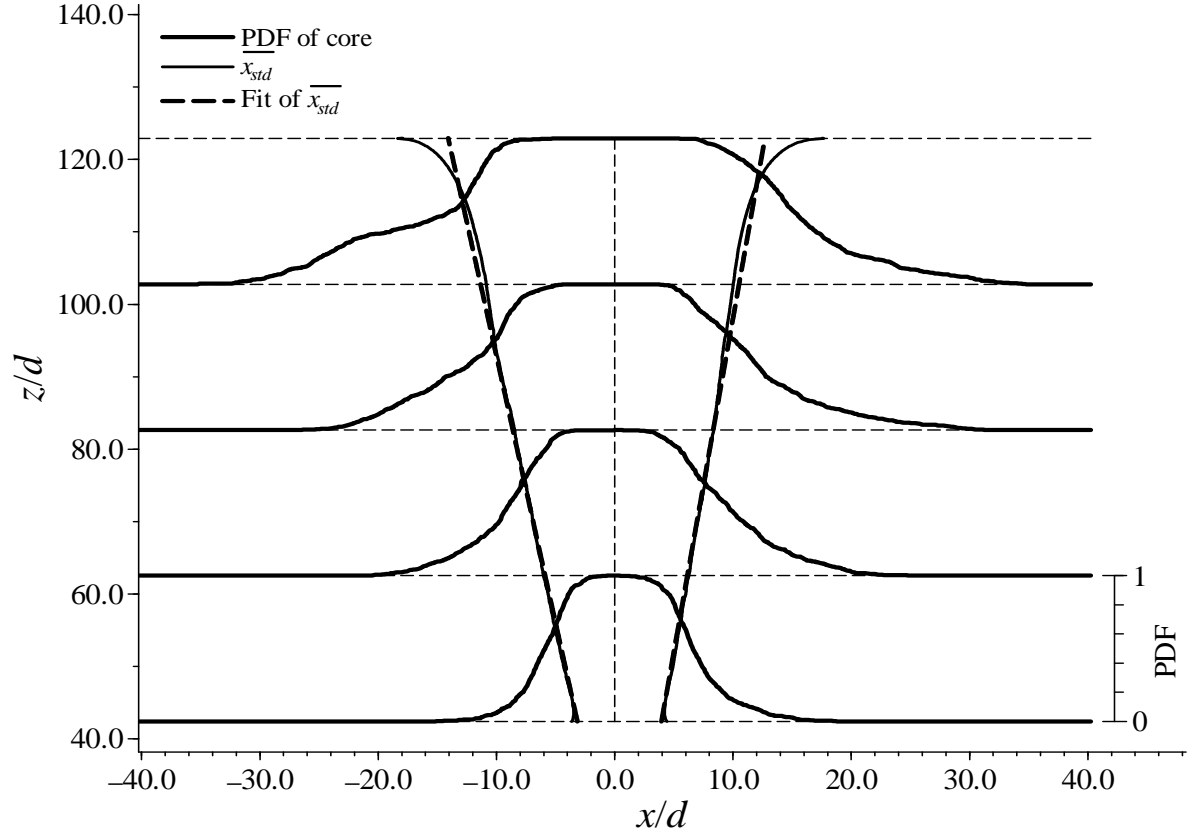


Figure 12: Time-averaged mean core structure in PIV study area 2. Probability density function or PDF (plotted with thick solid curves) of the core at different heights, data and linear fits of the time-averaged standard deviation $\overline{x_{std}}$ (plotted respectively with thin solid curves and dashed lines) of the core.

and vertical eddy standard deviations) located in the curves of the core structure and which carry some upward momentum flux (slightly less than a quarter of the total momentum flux in average).

The linear growth of the core shows that it is self-similar with height within the flow region studied, as we found for the eddies. The spatial statistical distribution of the location of the core is due to its particular wave-like dynamics. The undulations along the centreline of this high-velocity core are characterised by an essentially self-similar PDF. The standard deviation of the PDF increases with height at a rate of 0.12, which is quite close to the rate of change with height of the mean velocity spread rate $db/dz = 0.15$. The spatial Gaussian distribution of the time-averaged mean vertical velocity is therefore the result of the statistical spatial distribution of the undulating core. It is difficult to assess whether the eddies have a direct contribution to this statistical process. However, their role in the large-scale dynamics of the core is essential.

6 Conclusion

In this experimental study of quasi-two-dimensional turbulent jets (and similarly to Giger *et al.* (1991) and Dracos *et al.* (1992)) we have observed that the flow organises into a very interesting structure with a sinuous core of high vertical velocity oscillating about the centreline and eddies rising and growing along the undulations. As predicted by the theoretical model, we find that the mean velocity field measured with PIV is self-similar with height (see figure 14), the normalised time-averaged vertical velocity profile \bar{w}/\bar{w}_n (plotted with thick solid curves, and where \bar{w}_n is the maximum time-averaged vertical velocity at the lowest height, $\hat{z}_n = 42.4$) is close to a Gaussian distribution and the velocity peak decreases as $\hat{z}^{-1/2}$ with height. The return flow due to the lateral confinement of the jet could explain the small mismatch between the theory and the experimental results. Friction at the bounding walls has only a second-order effect on the momentum flux (of the order of 10% compared to the average value of the momentum flux) and thus on the velocity field. Within the flow region studied, we also find that both the eddies (average eddy paths plotted with dashed lines) and the core (time-averaged standard-deviation plotted with thin solid lines) are on average self-similar with height, which is not described by the theory and is fundamentally different from either a (fully unconfined planar) two-dimensional jet or a (fully unconfined non-planar) three-dimensional jet, where the turbulence is unconfined and three-dimensional.

The confinement of the jet in a narrow gap undoubtedly changes the structure of the turbulence in the flow with a quasi-two-dimensional inverse cascade allowing large eddies to grow. This persistent growth of eddies is contrary to three-dimensional turbulence. The eddies form within the intense shear layer at the boundary between the jet and the ambient flow when the width of the jet b is larger than the thickness of the flow W (Dracos *et al.*, 1992). Then, the eddy structures appear periodically at a given height. The eddy frequency decreases with height due to merging and we find a well-defined minimum Strouhal number $St \geq 0.07$. The dynamics of these eddies is strongly coupled with the dynamics of the core. The core, which moves on average four times faster and carries approximately 75% of the momentum flux, flows round the eddies. The consequence of these lateral excursions is seen in the mean velocity field. We believe that the unstable dynamics of the core characterised by its probability density distribution is responsible for the Gaussian profile of the time-averaged vertical velocity. In this flow, it is the two-dimensional macro-structure and not the three-dimensional small-scale turbulence which produces the Gaussian distribution.

Therefore, analysing the instantaneous flow field is key to understanding how entrainment, mixing and dispersion occur in the jet. The eddies play a leading role in the entrainment by engulfing ambient

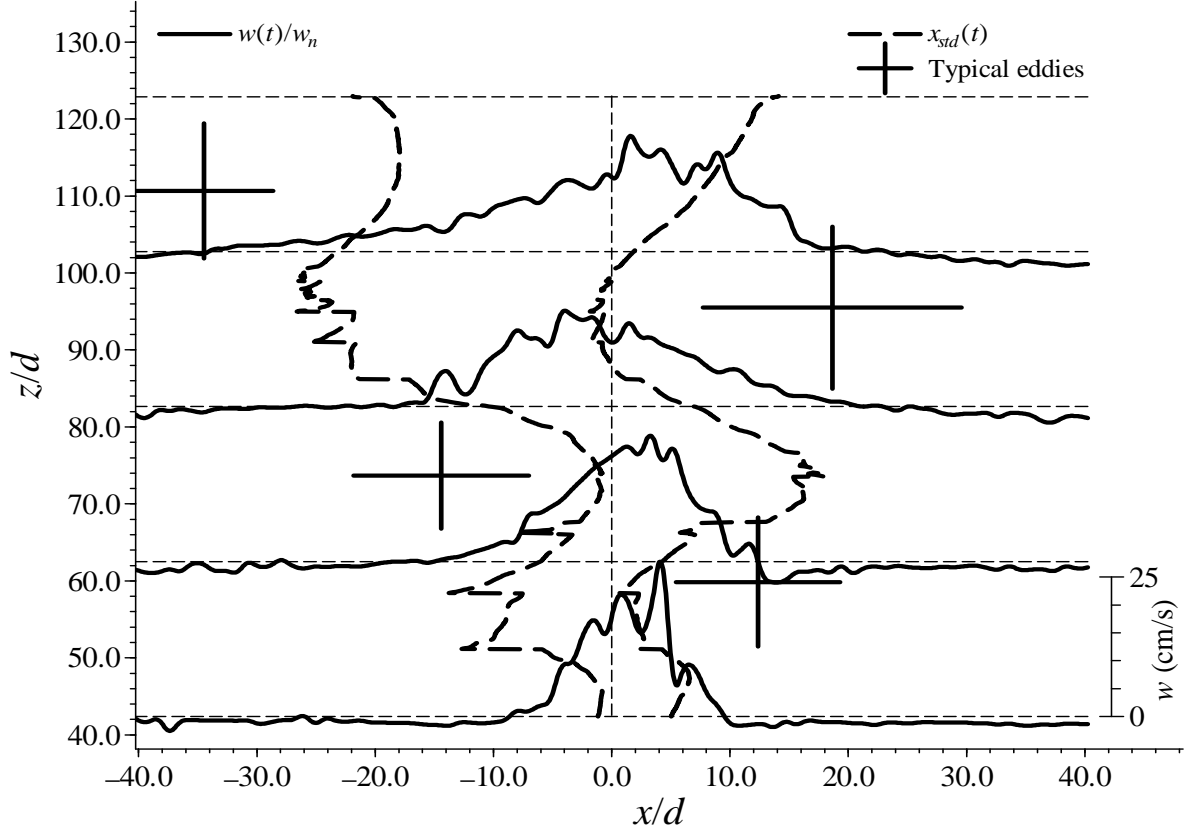


Figure 13: Distribution of the instantaneous normalised vertical velocity $w(t)/w_n$ (plotted with solid curves) at different heights and corresponding to the jet presented in figure 8(b). Instantaneous standard deviation $x_{std}(t)$ (plotted with dashed curves) of the core of the jet presented in figure 8(b) with its eddies (shown as crosses, with the size of the crosses representing the horizontal and vertical eddy standard deviations).

fluid at their rear, as we noticed from the study of the streamlines in the core and eddy structure. This entrainment mechanism ensures the linear growth of both the core and the eddies, therefore explaining the self-similarity of these structures. The exchange of fluid between the core and the eddies is permanent and in both directions as streamlines evolve in time from being closed within an eddy to being open and stretched in the core. It is perhaps surprising that the entrainment assumption of Morton *et al.* (1956), modelling entrainment due to three-dimensional turbulent mechanisms, can also describe the fundamentally different two-dimensional case. We find that the entrainment coefficient is $0.052 \leq \alpha \leq 0.068$, depending on how it is calculated. The dyed jet experiments revealed the vigorous mixing effect of the eddies. It is also worth noting that the average dye edge (shown with dotted lines in figure 14) coincides with the average outer boundaries of the eddies, which is the physical maximum lateral extent of the jet. Mixing is apparently not as strong in the core, but intense stretching leading to large vertical dispersion occurs at the interface with the eddies. This region is delimited between the thin solid lines and the dashed lines shown in figure 14.

In conclusion, a probabilistic description of the core–eddy structure of quasi-two-dimensional jets leads to a self-similar Gaussian description of the time-averaged flow. The instantaneous flow has a very different character from either (fully unconfined planar) two-dimensional flows or (fully unconfined non-planar) three-dimensional flows. Bulk long time-averaged properties are consistent with conventional theoretical models, but the mixing and dispersion cannot be accounted for by these time-averaged models. Future studies will investigate quantitatively the mixing, diffusion and vertical dispersion in such quasi-two-dimensional jets.

Acknowledgments This work has been funded through the BP Institute (BPI) and EPSRC. We gratefully acknowledge the technical assistance and advice of Dr S. Dalziel (DAMTP). J. R. L. would also like to thank his colleague S. Rabin (DAMTP) for fruitful discussions. Thanks are also due to A. Pluck (BPI), and D. Page-Croft and the technicians of the G. K. Batchelor Laboratory (DAMTP).

References

- ALBERTSON, M. L., DAI, Y. B., JENSEN, R. A. & ROUSE, H. 1950 Diffusion of submerged jets. *Transactions of the American Society of Civil Engineers* **115**, 639–664.
- ANTONIA, R. A., SATYAPRAKASH, B. R. & HUSSAIN, A. K. M. F. 1980 Measurements of dissipation rate and some other characteristics of turbulent plane and circular jets. *Physics of Fluids* **23**, 695–700.
- BIRD, R. B., STEWART, W. E. & LIGHTFOOT, E. N. 2007 *Transport phenomena. Second edition*. John Wiley & Sons, Inc.
- CHEN, D. & JIRKA, G. H. 1998 Linear stability analysis of turbulent mixing layers and jets in shallow water layers. *Journal of Hydraulic Research* **36**, 815–830.
- DE YOUNG, D. S. 1997 Growth of large scale structures in two-dimensional mixing layers. *Physics of Fluids* **9**, 2168–2170.
- DIMOTAKIS, P. E., MIAKE-LYE, R. C. & PAPANTONIOU, D. A. 1983 Structure and dynamics of round turbulent jets. *Physics of Fluids* **26**, 3185–3192.

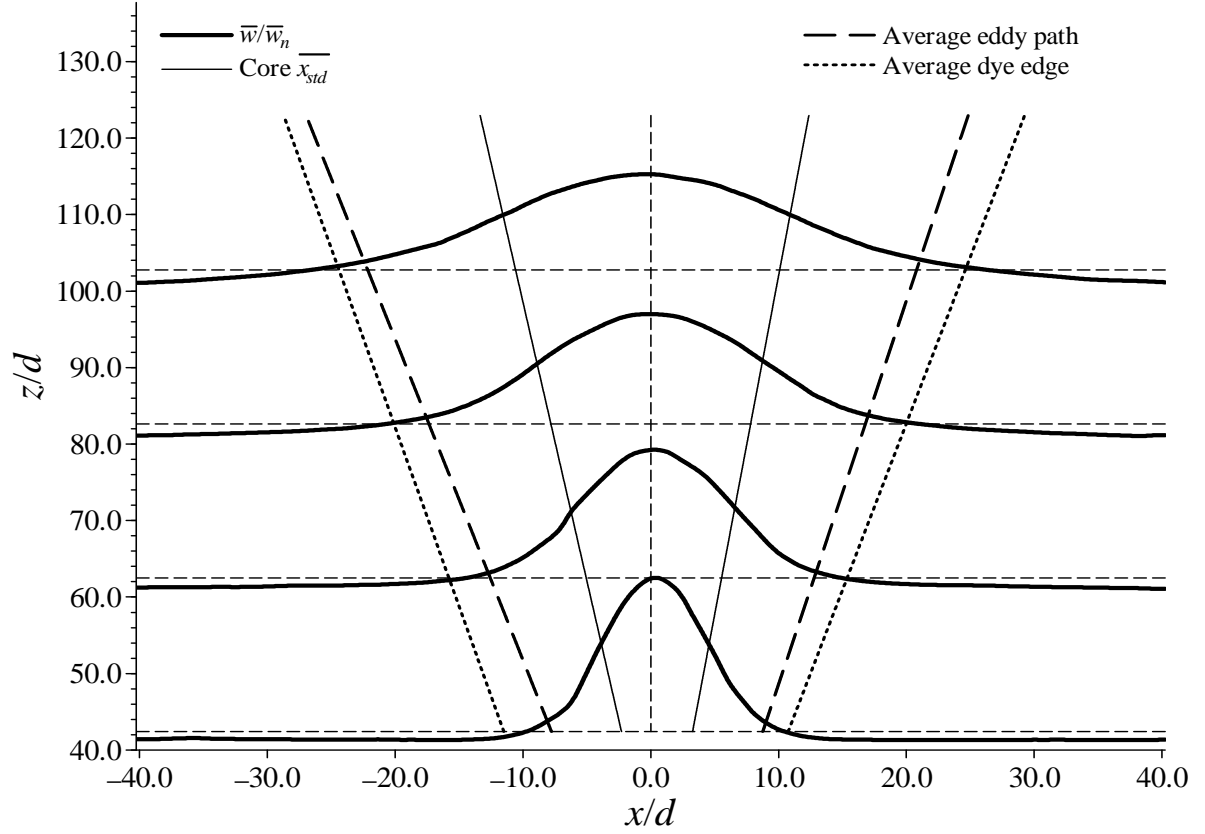


Figure 14: Distribution at different heights of: normalised time-averaged vertical velocity $\overline{w}/\overline{w}_n$ (plotted with thick solid curves); time-averaged standard deviation of the mean core \overline{x}_{std} (plotted with thin solid lines); ensemble-averaged mean trajectory of eddies (plotted with dashed lines); and average dye edge (plotted with dotted lines).

- DRACOS, T., GIGER, M. & JIRKA, G. H. 1992 Plane turbulent jets in a bounded fluid layer. *Journal of Fluid Mechanics* **241**, 587–614.
- DRAYTON, M. J. 1993 Eulerian and lagrangian studies of inhomogeneous turbulence generated by an oscillating grid. PhD thesis, University of Cambridge, Cambridge, UK.
- FOSS, J. F. & JONES, J. B. 1968 Secondary flow effects in a bounded rectangular jet. *Journal of Basic Engineering* **90**, 241–248.
- FUNG, J. C. H. 1990 Kinematic simulation of turbulent flow and particle motion. PhD thesis, University of Cambridge, Cambridge, UK.
- GIGER, M., DRACOS, T. & JIRKA, G. H. 1991 Entrainment and mixing in plane turbulent jets in shallow water. *Journal of Hydraulic Research* **29**, 615–642.
- CERVANTES DE GORTARI, J. & GOLDSCHMIDT, V. W. 1981 The apparent flapping motion of a turbulent plane jet—Further experimental results. *Journal of Fluids Engineering—Transactions of the ASME* **103**, 119–126.
- HOLDEMAN, J. D. & FOSS, J. F. 1975 Initiation, development, and decay of secondary flow in a bounded jet. *Journal of Fluids Engineering—Transactions of the ASME* **97**, 342–352.
- HUSSEIN, H. J., CAPP, S. P. & GEORGE, W. K. 1994 Velocity measurements in a high-Reynolds number, momentum-conserving, axisymmetric, turbulent jet. *Journal of Fluid Mechanics* **258**, 31–75.
- JIRKA, G. H. 2001 Large scale flow structures and mixing processes in shallow flows. *Journal of Hydraulic Research* **39**, 567–573.
- JIRKA, G. H. 2006 Integral model for turbulent buoyant jets in unbounded stratified flows. Part 2: plane jet dynamics resulting from multiport diffuser jets. *Environmental Fluid Mechanics* **6**, 43–100.
- JIRKA, G. H. & HARLEMAN, D. R. F. 1979 Stability and mixing of a vertical plane buoyant jet in confined depth. *Journal of Fluid Mechanics* **94**, 275–304.
- KOTSOVINOS, N. E. 1975 A study of the entrainment and turbulence in a plane buoyant jet. PhD thesis, California Institute of Technology, Pasadena, USA.
- KOTSOVINOS, N. E. 1976 A note on the spreading rate and virtual origin of a plane turbulent jet. *Journal of Fluid Mechanics* **77**, 305–311.
- KOTSOVINOS, N. E. & LIST, E. J. 1977 Plane turbulent buoyant jets. Part 1. Integral properties. *Journal of Fluid Mechanics* **81**, 25–44.
- KUANG, J., HSU, C.-T. & QIU, H. 2001 Experiments on vertical turbulent plane jets in water of finite depth. *Journal of Engineering Mechanics—ASCE* **127**, 18–26.
- LIST, E. J. 1982 Turbulent jets and plumes. *Annual Review of Fluid Mechanics* **14**, 189–212.
- MORTON, B. R., TAYLOR, G. I. & TURNER, J. S. 1956 Turbulent gravitational convection from maintained and instantaneous sources. *Proceedings of the Royal Society London, Serie A* **234**, 1–23.

- POPE, S. B. 2000 *Turbulent flows*. Cambridge University Press.
- RAMAPRIAN, B. R. & CHANDRASEKHARA, M. S. 1985 LDA measurements in plane turbulent jets. *Journal of Fluids Engineering—Transactions of the ASME* **107**, 264–271.
- ROBINSON, S. K. 1991 Coherent motions in the turbulent boundary layer. *Annual Review of Fluid Mechanics* **23**, 601–639.
- ROWLAND, J. C., STACEY, M. T. & DIETRICH, W. E. 2009 Turbulent characteristics of a shallow wall-bounded plane jet: experimental implications for river mouth hydrodynamics. *Journal of Fluid Mechanics* **627**, 423–449.
- SHINNEEB, A.-M., BUGG, J. D. & BALACHANDAR, R. 2011 Coherent structures in shallow water jets. *Journal of Fluids Engineering—Transactions of the ASME* **133**, 011203.
- SVEEN, J. K. & DALZIEL, S. B. 2005 A dynamic masking technique for combined measurements of PIV and synthetic schlieren applied to internal gravity waves. *Measurement Science and Technology* **16**, 1954–1960.
- THOMAS, F. O. & BREHOB, E. G. 1986 An investigation of large-scale structure in the similarity region of a two-dimensional turbulent jet. *Physics of Fluids* **29**, 1788–1795.
- WANG, H. W. & LAW, A. W.-K. 2002 Second-order integral model for a round turbulent buoyant jet. *Journal of Fluid Mechanics* **459**, 397–428.
- XU, H. & BODENSCHATZ, E. 2008 Motion of inertial particles with size larger than Kolmogorov scale in turbulent flows. *Physica D* **237**, 2095–2100.